Nanoscale

PAPER

View Article Online
View Journal | View Issue

Cite this: *Nanoscale*, 2025, **17**, 15267

Biological degradation of graphitic carbon nitride sheets and autophagy induction in macrophages†

K. Swetha,[a] Anushree Bhatnagar,[b] Manikrishna Lakavathu,[a] Penta Poornima,[c] Pratiksha Ganesh,[a] Adithi Kamath,[a] Srinivasa Reddy Bonam,[c,d] Srinivasa M. Srinivasula[b] and Rajendra Kurapati *[a,e]

Received 22nd February 2025,
Accepted 12th May 2025

DOI: 10.1039/d5nr00795j

rsc.li/nanoscale

Although metal-free graphitic-C_3N_4 was studied for potential applications in bioimaging, cancer therapy, *etc.*, its biodegradability and impact on immune modulation and autophagy induction have not yet been reported, which are essential for designing clinical applications. Herein, we studied the biodegradability of two types of g-C_3N_4 nanosheets (exfoliated and porous) using human myeloperoxidase (hMPO) derived from primary immune cells (neutrophils), the plant enzyme horseradish peroxidase (HRP) and the photo-Fenton reaction (PF, generating hydroxy radicals). Biodegradation was followed by analysis using electron microscopy and spectroscopic techniques, including Raman, X-ray photoelectron, UV-vis and fluorescence spectroscopy. The results confirmed that the g-C_3N_4 sheets could be degraded more effectively by hMPO than by HRP, with porous g-C_3N_4 showing higher degradability than exfoliated g-C_3N_4 due to the presence of oxygen groups. Next, the PF reaction was applied to analyse the degradation by-products using mass spectrometry, and the cytotoxicity of degradation products was assessed in comparison with pristine g-C_3N_4. Additionally, the impact of g-C_3N_4 on the autophagy induction in RAW264.7 macrophages were confirmed by the overexpression of the autophagy marker, LC3 protein, particularly in response to porous sheets. Finally, the immunomodulatory function of the nanosheets and cytokine production were evaluated in RAW macrophages following exposure to both porous and exfoliated g-C_3N_4. These findings demonstrated that porous nanosheets induced a dose-dependent pro-inflammatory response.

Introduction

The discovery of graphene has led to the development of a wide range of two-dimensional materials (2DMs), including graphene derivatives such as graphene oxide (GO) and reduced graphene oxide (rGO), transition metal dichalcogenides (*e.g.*, MoS_2), hexagonal boron nitride (h-BN), monoelemental materials (phosphorene), and transition metal carbides or nitrides (MXenes).[1] Though 2DMs are being used in many industrial applications, including biomedical applications, the impact (nano-safety) of such materials and their *in vivo* (biological) and environmental degradation to understand the implications of such emerging materials studied.[2] However, the cytotoxicity of these materials has been mainly studied, with limited understanding of their biological or environmental degradation. To date, the biodegradation of graphene family materials (GFMs), including GO,[3,4] rGO,[5] nanoribbons[6] and graphene,[7] were studied. Biodegradation of GFMs has mainly been demonstrated through enzymatic catalysis by peroxidases isolated from immune cells, such as myeloperoxidase (MPO)[4,6–9] and eosinophil peroxidase (EPO),[10,11] along with inducible nitric oxide synthase (iNOS).[5,9,12,13] Furthermore, biodegradation of GFMs has been demonstrated using the plant enzyme, horseradish peroxidase (HRP), and microbial secreting enzymes such as lignin peroxidase (LiP), laccase, *etc.*[14] Biological and environmental degradation of inorganic 2DMs, including MoS_2, h-BN, and antimonene sheets, were also reported.[8,15–17]

Recently, graphitic carbon nitride (g-C_3N_4) has received wide attention due to its unique characteristics,[18] including

[a]*School of Chemistry, Indian Institute of Science Education and Research Thiruvananthapuram, Maruthamala P.O., Vithura, Thiruvananthapuram, Kerala 695551, India. E-mail: rkurapati@iisertvm.ac.in*
[b]*School of Biology, Indian Institute of Science Education and Research Thiruvananthapuram, Maruthamala PO, Vithura, Thiruvananthapuram 695551, Kerala, India*
[c]*Vaccine Immunology Laboratory, Department of Applied Biology, CSIR-Indian Institute of Chemical Technology, Hyderabad 500007, Telangana, India*
[d]*Academy of Scientific and Innovative Research, Ghaziabad 201002, India*
[e]*The Centre for Advanced Materials Research with International Engagement, (CAMRIE), Indian Institute of Science Education and Research Thiruvananthapuram, Maruthamala P.O., Vithura, Thiruvananthapuram, Kerala 695551, India*
† Electronic supplementary information (ESI) available. See DOI: https://doi.org/10.1039/d5nr00795j

optical properties, a tunable band gap, high chemical stability and facile synthesis.[19] Furthermore, g-C_3N_4 exhibits fluorescence as an n-type semiconductor consisting of alternating sp^2-hybridized C and N atoms forming the triazine.[20–22] g-C_3N_4 has many promising biomedical applications owing to its low toxicity and high fluorescence compared to other 2DMs, especially graphene, making g-C_3N_4 a unique candidate for *in vivo* bioimaging and photothermal therapies.[22] However, the biodegradability of such g-C_3N_4 has not yet been reported, which is crucial for understanding it is *in vivo* fate and for designing potential biomedical applications.

On the other hand, investigating nano-immune interactions has attracted attention due to the impact of 2D materials in inducing autophagy (*i.e.*, the self-defensive mechanism of cells where organelles or unwanted proteins are recycled) and their immune modulation properties, which have potential applications in nano-immunotherapies (cancer therapies).[23] 2D materials, such as GO and h-BN sheets, were found to induce autophagy in cancer cells.[24–26] Investigating such nano-immune interactions with g-C3N4 sheets could be interesting in understanding potential applications in autophagy induction and cancer therapies.

Herein, we study the biodegradation of exfoliated (Exf) and porous (Por) g-C_3N_4 sheets by human peroxidase (hMPO), a plant peroxidase (HRP) and photo-Fenton's reaction (PF, generating hydroxy radicals). The degradation of g-C_3N_4 was followed by characterization using electron microscopy and various spectroscopic methods; in addition, degradation by-products after the PF reaction were identified. Next, the induction of autophagy in RAW264.7 macrophages were analysed by incubating with g-C_3N_4. Finally, the cytokine production was evaluated in RAW264.7 macrophages to understand any immunomodulatory functions of g-C_3N_4 nanosheets.

Results and discussion

Synthesis of exfoliated and porous g-C_3N_4 nanosheets

First, the Exf g-C_3N_4 nanosheets were prepared using aqueous exfoliation *via* ultrasonication of bulk g-C_3N_4 for 16 h.[19] Next, the Por g-C_3N_4 sheets were obtained by the acid treatment (oxidation) of bulk g-C_3N_4 using $K_2Cr_2O_3$ in H_2SO_4, followed by sonication for 2 h to increase the oxygenated groups (carboxyl and hydroxyl).[27] As prepared, Exf and Por g-C_3N_4 sheets were characterized using different spectroscopic and microscopic techniques. HR-TEM images confirm the formation of exfoliated g-C_3N_4 (Fig. 1A), as seen from the flat and thin sheets. In contrast, Por g-C_3N_4 sheets show many pores with rough morphology (Fig. 1B); additional images are shown in (Fig. S1, ESI†).[19,27] The average size distribution of the Exf and Por sheets was 252.2 ± 195.5 nm (~25 sheets) and 402.7 ± 287.8 (~pore size of 109.8 ± 59.8), respectively. Further, AFM analysis (Fig. S2†) revealed that the thickness of the Exf sheets was 5 nm while that of Por sheets varied from 2 to 3 nm, suggesting the porous morphology of the sheets. Additionally, increased colloidal stability was observed for Por g-C_3N_4 (zeta potential = −30.9 ± 4 mV) over Exf sheets (ζ = −23.0 ± 3.8 mV), attributed to the presence of a more significant number of carboxyl and hydroxyl groups introduced after chemical exfoliation for porous sheets (Fig. S3†). Next, the Raman analysis (Fig. S4†) confirmed the exfoliation of bulk g-C_3N_4 into the thin sheets due to the presence of two new peaks at 708 and (breathing mode of triazine), and the peak at 1234 cm^{-1} (C═N sp^2 bending vibration) corresponds to the quantum confinement effect from thin g-C_3N_4 sheets.[19] Also, Por sheets showed a defect peak of C–OH (1257 cm^{-1}, in-plane bending mode in C–OH) and the N–C–N stretching is more prominent in Por g-C_3N_4 due to more sp^3 C–N bonds.[28] Further, UV-visible (Fig. S5A†), X-ray diffraction (Fig. S5B†) and fluorescence spectroscopy (Fig. S5C†) also confirmed the formation of g-C_3N_4 sheets. All these results confirmed the successful synthesis of Exf and Por g-C_3N_4 sheets.

Biodegradability of porous and exfoliated g-C_3N_4 sheets

Biodegradation of g-C_3N_4 is crucial for understanding it is *in vivo* fate, which will enable the design of better potential applications, such as bioimaging, photothermal cancer therapies, *etc*. In this regard, both Exf and Por g-C_3N_4 nanosheets were incubated with human MPO, plant HRP and the UV-assisted PF reaction to assess their biodegradability, as shown in Fig. 1C. Neutrophils secrete MPO upon activation to fight against microbes and foreign bodies by generating a highly efficient oxidant NaOCl.[29] Hence, probing the biodegradability of g-C_3N_4 by MPO will be interesting in understanding its degradability and possible degradation by-products. First, hMPO (from neutrophils) was incubated with *Exf*- and *Por*-g-C_3N_4 nanosheets in the presence of lower concentrations of H_2O_2 for 60 h, where hMPO and H_2O_2 were renewed every 5 h and 1 h, respectively. The biodegradation of both g-C_3N_4 sheets was monitored using TEM and Raman spectroscopy for aliquots at different time points. First, the HR-TEM analysis showed distinct changes in the morphology of Exf g-C_3N_4 after a 60 h incubation compared to 0 h (Fig. 2A and B), where completely distorted sheets with nanoscale pores were observed (Fig. 2C and D). Por g-C_3N_4 sheets displayed a more destructed morphology (Fig. 2G and H) consisting of larger pores and the absence of sheet-like morphology after the 60 h hMPO treatment compared to the 0 h sample (Fig. 2E and F). Next, to support the TEM results, Raman analysis of g-C_3N_4 was performed after hMPO treatment (Fig. 2I and J). The intensity of the characteristic peaks of Exf g-C_3N_4 decreased after 60 h, which could be due to the oxidation of g-C_3N_4 nanosheets.[30] In the case of porous sheets, the distinct peaks at 708, 756, 978 and 1240 cm^{-1} were found with much lower intensity and broadened after the 60 h treatment, which demonstrated that higher oxidation was possible in Por g-C_3N_4 compared to exfoliated sheets. This higher degradation of Por g-C_3N_4 could be due to pre-existing oxygen-containing groups and pores on its surface that could act as potential sites to initiate the oxidation/degradation process similar to those in graphene oxide.[31,27] The Raman analysis correlates with the morphological changes observed in the TEM analysis. Overall, Raman

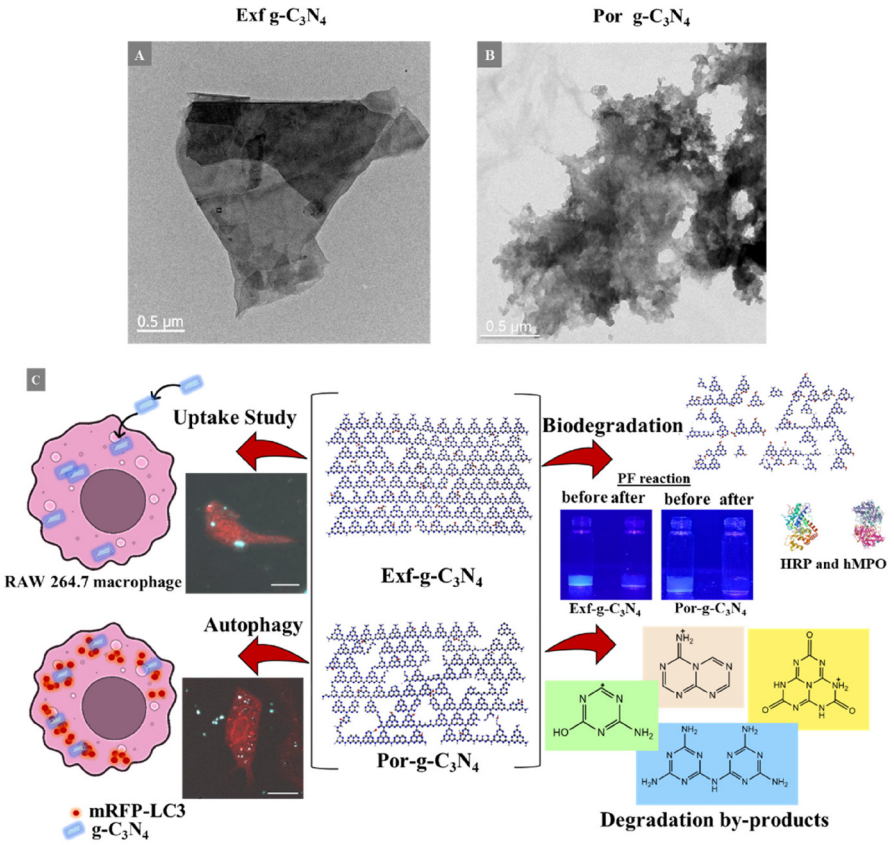

Fig. 1 (A) and (B) TEM images of Exf and Por g-C_3N_4 sheets. (C) Structural representation of the Exf and Por g-C_3N_4 sheets and their degradation after treatment with hMPO (human), HRP (plant) and PF reaction (radical environment). The vials (under UV light, 365 nm) containing Exf and Por g-C_3N_4 sheets before (0 h) and after the PF reaction (150 h) are shown on the right-hand side, along with the possible degradation by-products. Confocal images are shown (left-hand side) after treatment with the Exf and Por g-C_3N_4 sheets, depicting the uptake and autophagy (schematic representation).

spectroscopy and HRTEM analyses confirmed the oxidation of Exf and Por g-C_3N_4 nanosheets after treatment with hMPO for 60 h.

Further, to understand the environmental degradability of g-C_3N_4 sheets, a plant peroxidase (HRP) was treated with the nanosheets for 60 d in the presence of H_2O_2, where HRP was renewed every 20 d and H_2O_2 was added every 24 h. Next, TEM and Raman analyses was performed on aliquots collected at 0, 20, 40 and 60 d to track the degradation of both Exf and Por g-C_3N_4 sheets. Almost complete damage was observed for the morphology of the g-C_3N_4 sheets for the Exf g-C_3N_4 sheets after 60 d compared to the 0 d sheets (Fig. S6†). The sheet morphology of Exf g-C_3N_4 was drastically changed, consisting of several nanoscale pores and rough edges (Fig. S6C and D†), after the 60d treatment, unlike the flat sheets found at 0 d. Por g-C_3N_4 sheets displayed large pores after 60 days (Fig. S6G and H†), indicating complete damage to the g-C_3N_4 sheets compared to 0 day sheets (Fig. S6E and F†). Next, the Raman analysis confirmed significant changes in the Raman spectra of both the Exf and Por g-C_3N_4 sheets after 40 and 60 days of treatment (Fig. S6I and J†). In the case of Exf g-C_3N_4 nanosheets, the characteristic peaks were quite intense, corresponding to the distinct triazine structure of g-C_3N_4 sheets.[30] After the 40 d treatment, two types of Raman spectra were obtained for both Exf and Por g-C_3N_4 (Fig. S6I and J†) owing to the non-uniform degradation of the samples. The type I plot at 40 d could be attributed to the less degraded regions of g-C_3N_4 sheets, as the characteristic peaks are comparatively more intense and discrete. However, the type II plots (40 d) display very feeble and broad characteristic peaks that could correspond to the highly oxidized or degraded regions, similar to the 60 day degradation plots. This kind of non-uniform degradation was reported previously for graphene samples treated with HRP due to the low dispersibility in the buffer for 60 days of incubation.[7] However, no visible distinct characteristic peaks were observed for both the g-C_3N_4 samples after 60 days, indicating complete degradation or oxidation of the nanosheets by the enzymatic action of HRP. Notably, Exf g-C_3N_4 sheets showed less degradability than porous sheets due to the pre-existing oxygen groups and pores on their surface that could initiate and propagate the oxidation reaction. Both hMPO and HRP-mediated enzymatic catalysis were found to have the potential to degrade the chemically stable g-C_3N_4 sheets, more significantly, the porous sheets. These

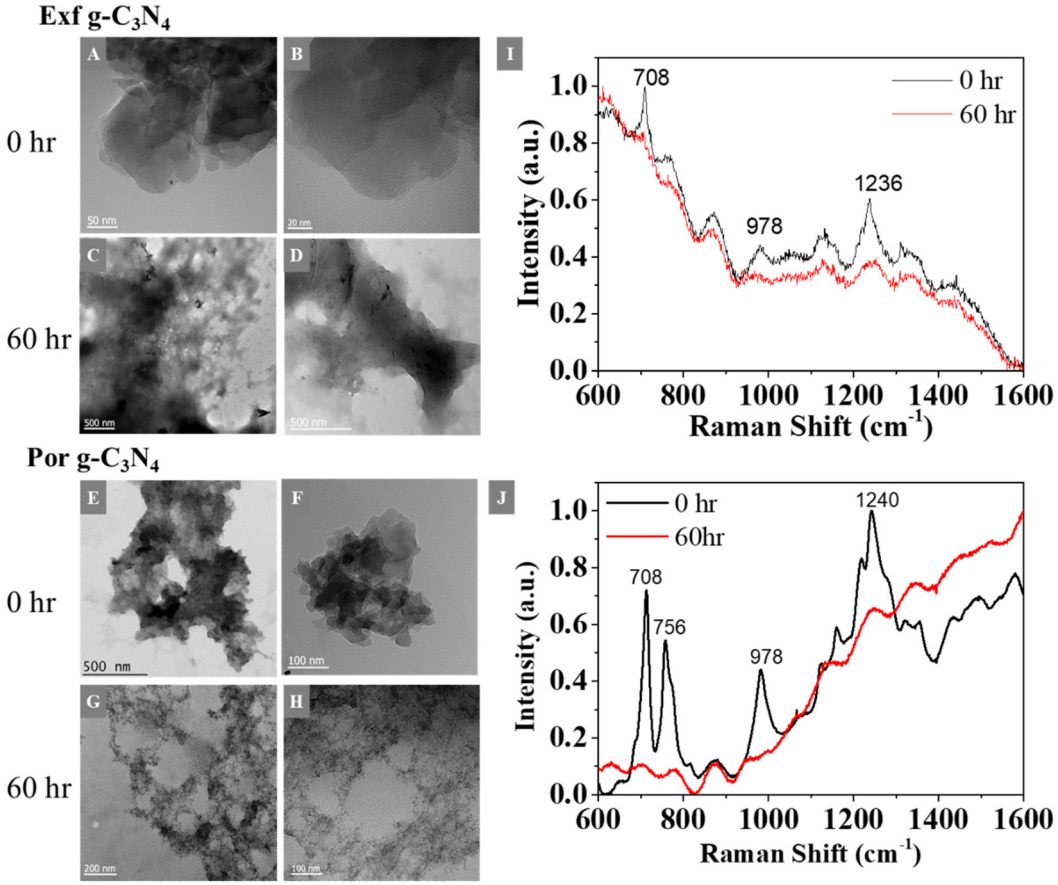

Fig. 2 TEM analyses of Exf 0 h (A and B) and 60 h (C and D), along with Por 0 h (E and F) and 60 h (G and H) g-C_3N_4 nanosheets treated with MPO. Raman spectroscopic analyses of exfoliated (I) and porous (J) g-C_3N_4 nanosheets (60 h sample).

results correlate with the degradation of other graphitic materials, including GO and graphene.[2]

PF reaction: degradation products and their cytotoxicity

Along with the peroxidase-catalyzed reactions, the UV-assisted PF reaction (generating hydroxyl radicals from H_2O_2 in the presence of $FeCl_3$/UV-light at pH 4) is readily applied to understand the extent (mechanism) of degradation of graphitic materials and the possible degradation by-products.[6,32] In addition, the PF reaction also mimics the oxidative stress that occurs in mitochondria, thereby generating HO$^{\bullet}$ radicals. PF was employed to assess the complete degradation of both Exf and Por g-C_3N_4 under UV light for 150 h (see ESI† for more details). The aliquots of PF-treated g-C_3N_4 at different time points were analyzed using Raman, UV-vis, fluorescence spectroscopy and HR-TEM (Fig. 3). First, HR-TEM analysis of the PF-treated Exf g-C_3N_4 after 150 h (Fig. 3D and E) showed drastic changes in the morphology than at 0 h (Fig. 3A and B). There was no visible sheet-like morphology, and numerous pores were observed after a 150 h treatment. Similar results were also obtained in the case of Por g-C_3N_4 sheets (Fig. 3J and K). Further, after the 150 h treatment, the Por g-C_3N_4 sheets completely lost their sheet morphology, and large-sized cavities were observed, along with considerable debris, unlike at 0 h (Fig. 3G and H). TEM analysis of control samples of both Exf and Por g-C_3N_4 (adding H_2O_2 without $FeCl_3$) showed no significant changes in their morphology after the 150 h treatment (Fig. S7A†). Similarly, Por g-C_3N_4 sheets were aggregated without any damage to the morphology of the sheets in the control samples after 150 h (Fig. S7B†). These results confirmed the need for the generation of hydroxy radicals to initiate the oxidation of the chemically resistant g-C_3N_4 sheets.

Further analysis of Exf and Por g-C_3N_4 nanosheets after the PF reaction was performed using UV-vis absorbance (Fig. 3C & I), where the spectra showed a significantly lower intensity, along with a disappearance of characteristic peaks of Exf g-C_3N_4 (329 nm) and Por g-C_3N_4 (318 nm) after 150 h. These results implied that the nanosheets had undergone chemical oxidation, leading to degradation. Similarly, the fluorescence intensity of Exf g-C_3N_4 and Por g-C_3N_4 was decreased by ~5 times and ~4 times, respectively, after the PF reaction of 150 h (Fig. 3F & L). A significant reduction in fluorescence of both Exf and Por g-C_3N_4 dispersions after 150 h was observed after illuminating the samples with long wave UV at 365 nm (insets of Fig. 3F & L), thereby indicating the structural destruction of

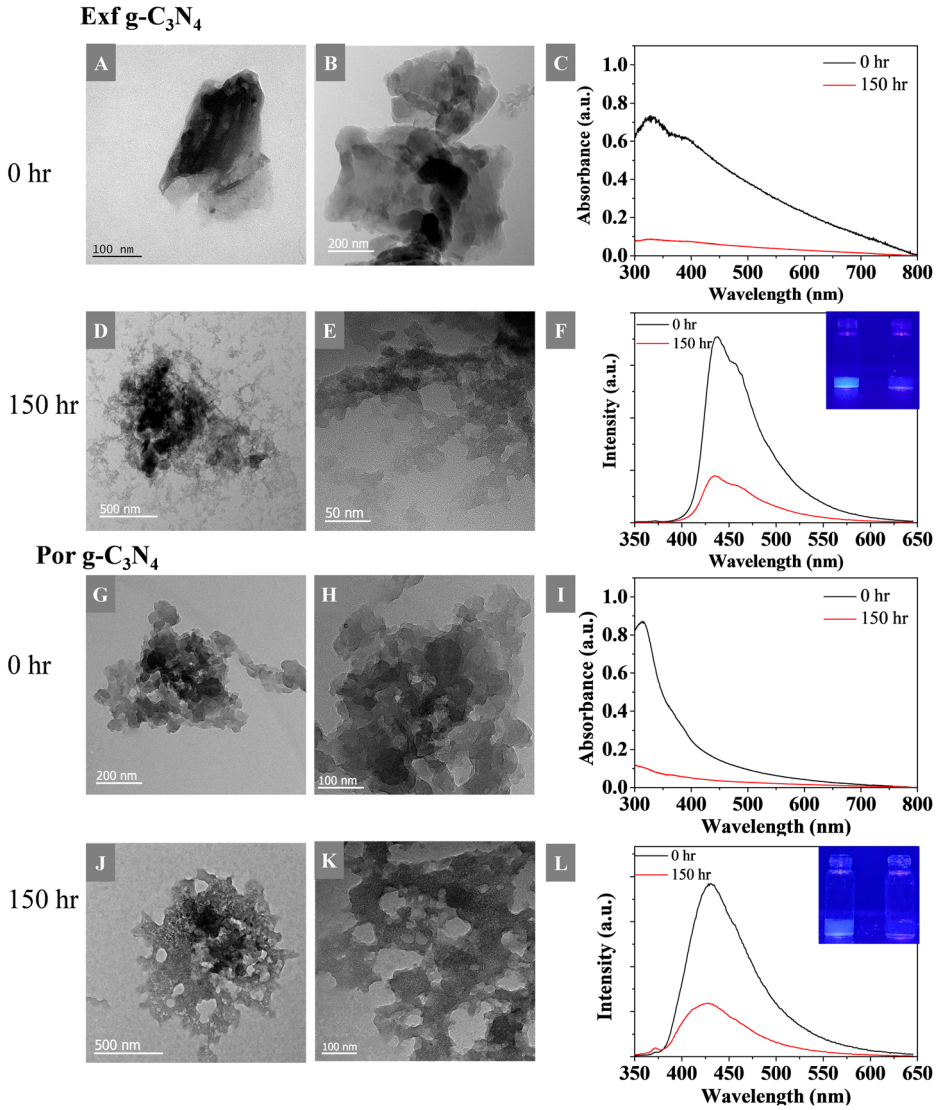

Fig. 3 TEM analysis of Exf g-C_3N_4 sheets at 0 h (A and B) and 150 h (D and E), along with Por 0 h (G and H) and 150 h (J and K) g-C_3N_4 sheets after the PF reaction. UV-vis spectra of Exf (C) and Por(I) g-C_3N_4 sheets. Fluorescence spectra of Exf g-C_3N_4 (F) and Por g-C_3N_4 (L), along with the photographs of Exf and Por g-C_3N_4 dispersions before and after PF degradation (in water as solvent at pH 4) illuminated with a long wave UV of 365 nm (insets).

g-C_3N_4 sheets. Further, Raman analysis (Fig. S8†) of the g-C_3N_4 sheets after the PF reaction shows no characteristic peaks corresponding to the CN heterocycle vibration modes, suggesting that the triazine structure of g-C_3N_4 may be significantly affected due to oxidation by $HO^{\bullet}$ radicals. Further, the X-ray photoelectron spectroscopy (XPS) analysis confirmed the drastic oxidation of g-C_3N_4 sheets, as a higher oxygen content was detected for both Exf and Por g-C_3N_4 sheets compared to untreated samples (Fig. 4A–D). Notably, the % of C and N in PF-treated Exf g-C_3N_4 sheets was reduced to 38.8% from 50.4 and 6.2 from 46.8, respectively, while the O% increased drastically to 54.9 from 2.7. Surprisingly, for the PF-treated Por g-C_3N_4, C% increased to 60 from 35.2, and N% was reduced to 1.5 from 51.9. However, there was a significant increase in O% (12.9 to 38.5), indicating the drastic doping of oxygen into the g-C_3N_4 structure or chemical oxidation. The unexpected increase in the C% for Por g-C_3N_4 sheets (after 150 h) might be attributed to the formation of amorphous carbon and small fragments of highly oxidised/damaged g-C_3N_4 sheets after the PF treatment for 150 h. Further, deconvoluted spectra of C 1s of both Exf and Por g-C_3N_4 sheets displayed two distinct peaks with maxima at ~288 and ~284 eV before the PF treatment corresponding to the sp^2 C–N units in the triazine moiety (Fig. 4E & G).[33,34] However, after 150 h, those two distinct peaks had disappeared and a single peak corresponding to oxygenated carbon was observed. The peaks for phenolic (C–OH), carbonyl (C=O), and carboxyl –COOH groups emerged after the 150 h treatment (Fig. 4F & H) compared to the 0 h samples. Moreover, the deconvoluted N 1s spectra (Fig. S9†) of the 150 h treated Exf g-C_3N_4 showed a peak at 398 eV with

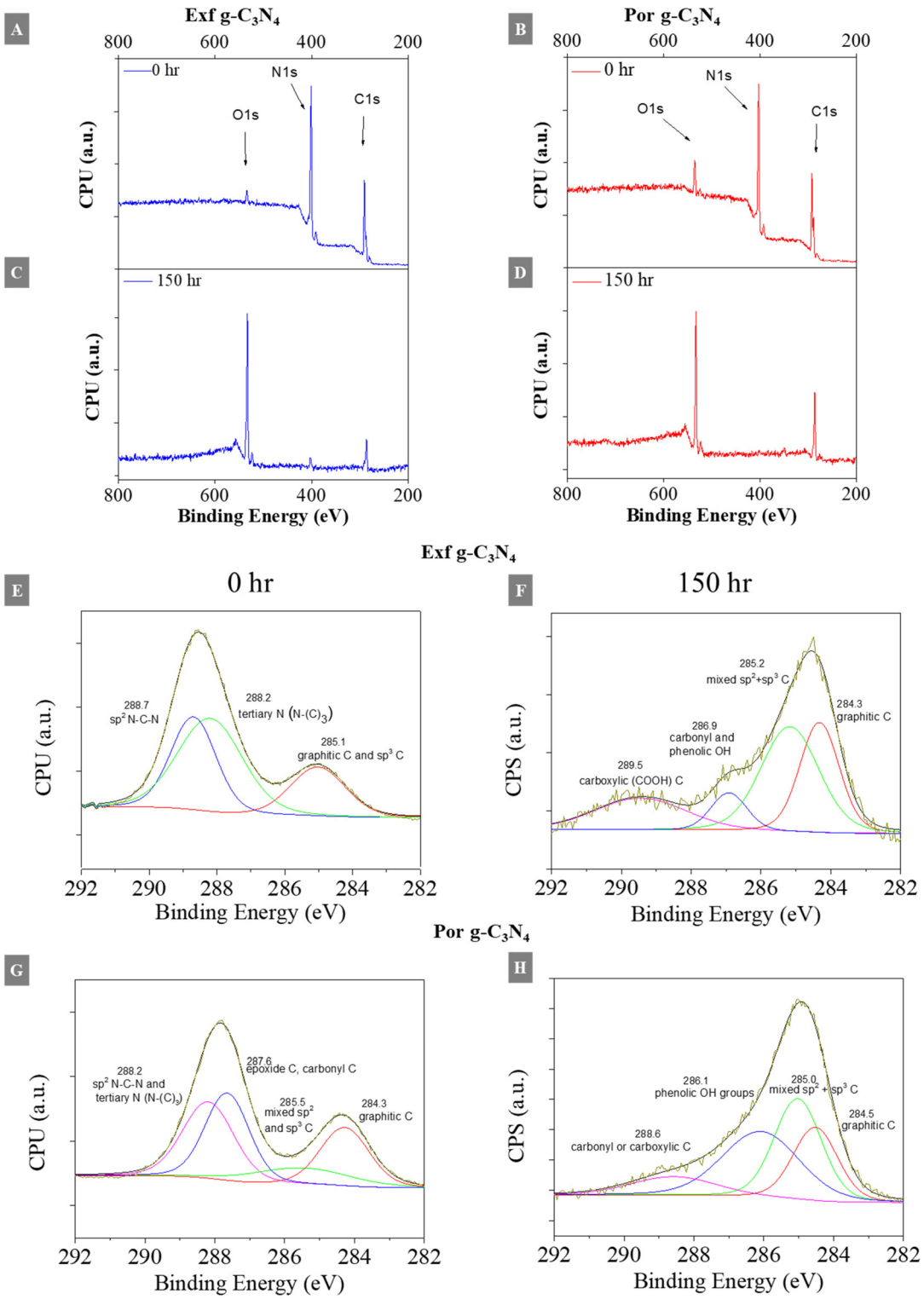

Fig. 4 XPS survey spectra of 0 h (A) and 150 h (C) degraded Exf, along with 0 h (B) and 150 h (D) degraded Por g-C_3N_4 nanosheets, respectively, mediated by the UV-catalysed photo-Fenton reaction. Deconvoluted C1s spectra for Exf and Por g-C_3N_4 nanosheets before (E and G, respectively) and after degradation using the PF reaction for 150 h (F and H, respectively).

lower intensity, suggesting a low amount of aromatic imine and a high-intensity peak at 403 eV, which corresponds to oxygen-containing moieties (N–(C═O)–O). However, Por g-C_3N_4 shows negligible N 1s spectra after the 150 h treatment (Fig. S9D†), possibly due to the more drastic oxidation of the porous sheets compared to Exf g-C_3N_4.

All these results confirmed that the PF treatment caused the highest degradation/oxidation of both g-C_3N_4 compared to peroxidase catalysis (hMPO or HRP). This could be due to the generation of strong oxidants like HO$^{\bullet}$ radicals during the PF reaction, with the highest oxidation potential of 2.31 V.[32] However, hMPO generates oxidants like HOCl with an oxidation potential of 1.48 V, along with enzyme radical intermediates, compound I (1.16 V) and compound II (1.34 V).[8] HRP generates enzymatic radical intermediates with much lower oxidation potential (~0.9 V), which takes more extended time and is less efficient to degrade or oxidize the g-C_3N_4 sheets than hMPO and the PF reaction.

Next, mass spectrometry was employed to identify the possible degradation by-products after PF treatment (Fig. 5) for both g-C_3N_4 sheets. Some plausible by-products were identified (Fig. 5C & D), where the peak at *m*/*z* 127 is identified as protonated melamine ($C_3N_6H_7^+$), which further fragmented at *m*/*z* 111 ($C_3N_4OH_3^+$), 97 ($C_3N_4H_5^+$), 85 ($C_2N_4H_5^+$), and 74 ($C_2N_2OH_5^+$).[35] The peaks at *m*/*z* 127 ($C_3N_6H_7^+$) and 236 ($C_6N_{11}H_{10}^+$) are separated by 109 mass units, indicating the dimerization of melamine. The dimer is commonly referred to as melam (235 Da) and is known to be a product of the thermal condensation of melamine.[36] The peaks at *m*/*z* 295, 279, and 262 are products of melam with different functional groups formed during oxidation. The peak at *m*/*z* 222 corresponds to cyameluric acid, a trihydroxy derivative of melem.[37] Further fragmentation of melem derivatives occurs due to the loss of the cyanamide group, which gives the double-ringed structure. The peaks at *m*/*z* 149 and 206 are products with different functional groups formed during oxidation. However, Por g-C_3N_4 itself is an oxidized form of exfoliated sheets. There are certain peaks in Por g-C_3N_4 0 h that were present in the degraded Exf g-C_3N_4 samples, which could be attributed to the fact that Por g-C_3N_4 sheets were synthesized by chemical oxidation, followed by exfoliation of bulk g-C_3N_4.

Cytotoxicity and autophagy study of porous and exfoliated g-C_3N_4 sheets on macrophage cells

Investigating degradation by-products and their potential cytotoxicity is crucial in understanding the long-term impact of g-C_3N_4 sheets when exposed to humans. In this regard, the cytotoxicity of both Exf and Por g-C_3N_4 sheets and their degradation by-products (after 150 h PF treatment) was determined using a well-known MTT cell viability assay.[38] Herein, different concentrations of g-C_3N_4 sheets were incubated with murine macrophages (RAW264.7), and MTT results (Fig. 6A) confirmed that Por g-C_3N_4 showed more than 75% cell viability even before and after degradation at almost all concentrations. However, after degradation, a slight decrease in cell viability was observed for 30 μg mL^{-1} Por g-C_3N_4 nanosheets. Further, the MTT assay results confirmed that Exf g-C_3N_4 sheets (Fig. 7A) exhibited higher cytotoxicity (~60% cell viability) than

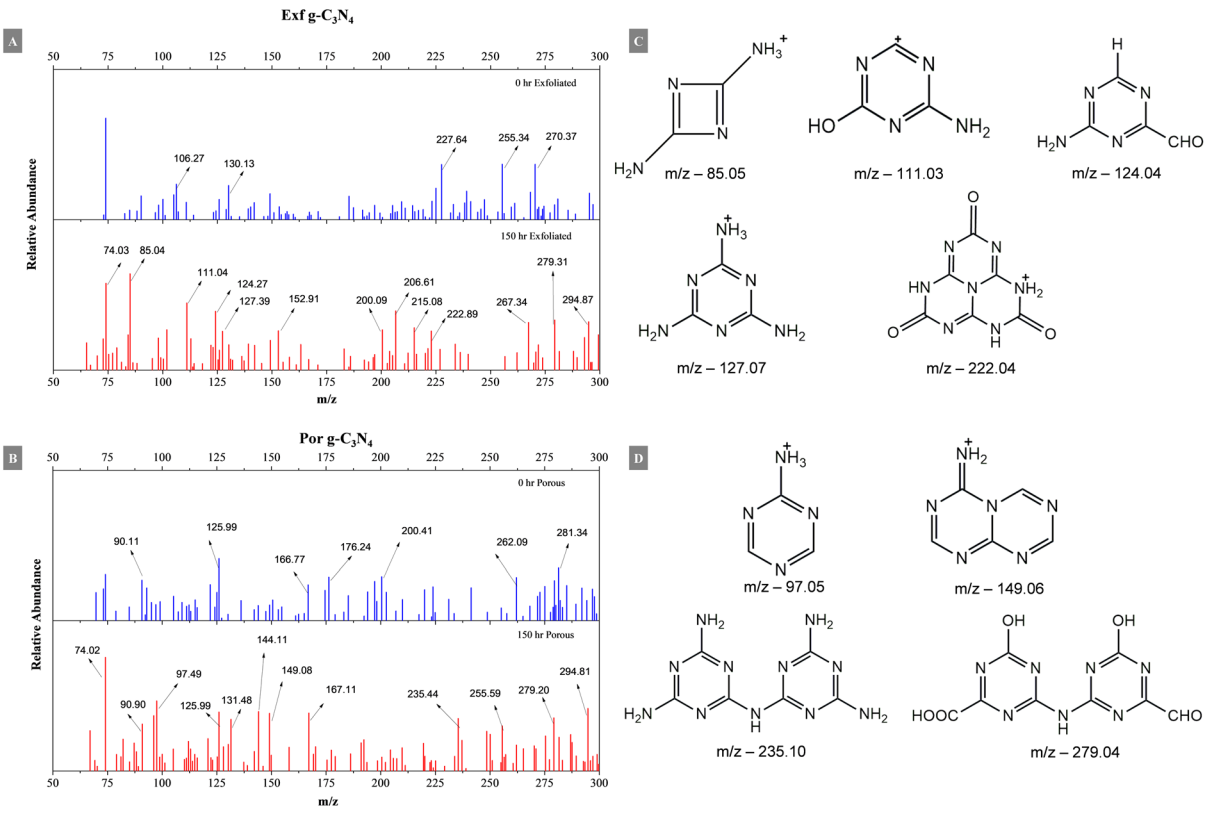

Fig. 5 Mass (LRMS) analyses of Exf (A) and Por (B) g-C_3N_4 nanosheets before and after degradation using the PF reaction for 150 h. The plausible degradation by-products of Exf g-C_3N_4 nanosheets (C) and Por g-C_3N_4 nanosheets (D) were analysed using mass spectrometry.

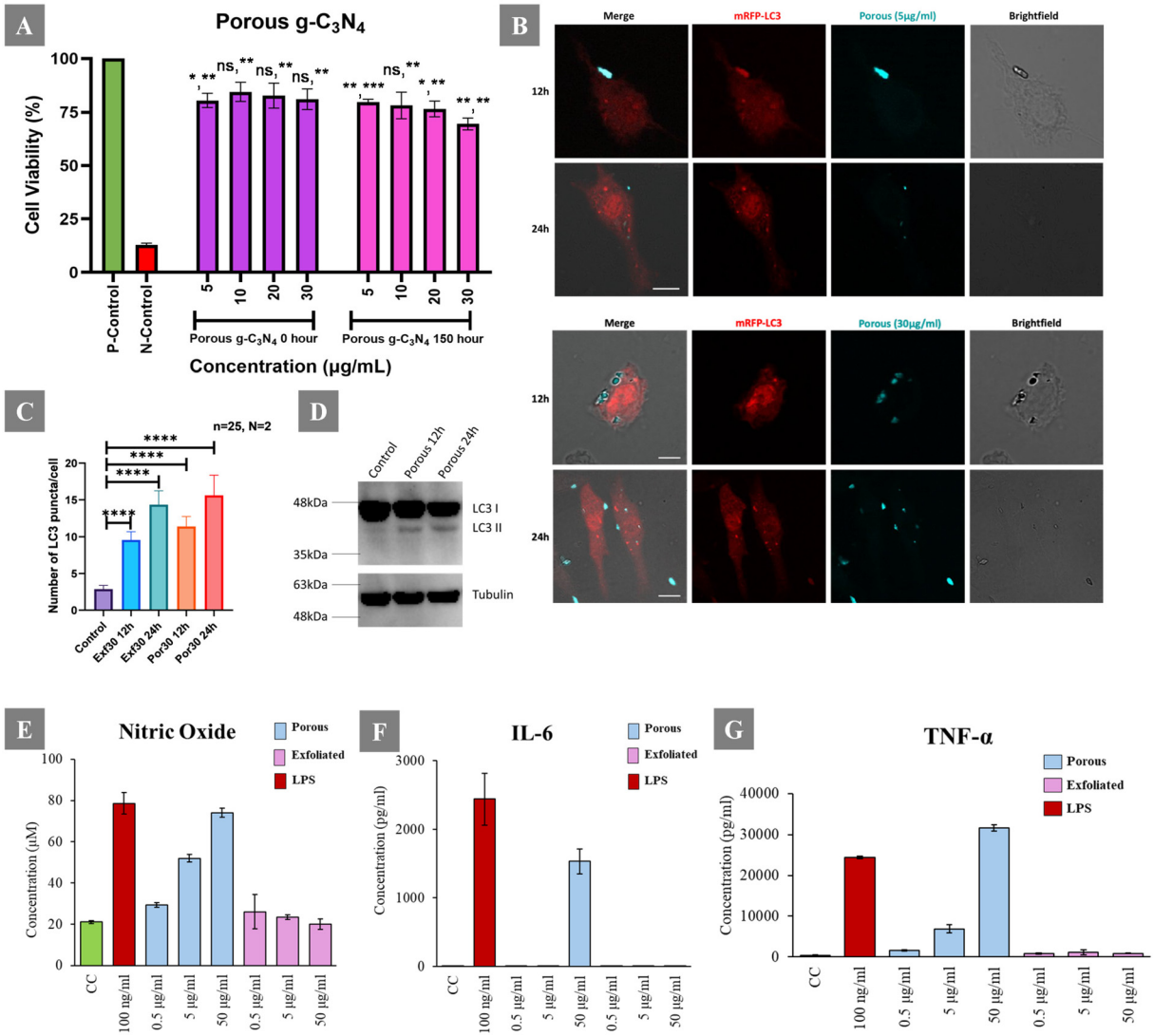

Fig. 6 (A) Cytotoxicity MTT study of Por g-C_3N_4 before and after degradation at four different concentrations 5, 10, 20, and 30 µg mL^{-1} performed on RAW264.7 macrophages. Data are shown as mean ± SEM. Statistical significance was tested with a two-tailed, paired Student's test, which is represented for each concentration *vs.* positive control (left side) and each concentration *vs.* negative control (right side). *P < 0.05, **P < 0.01, ***P < 0.001, and ns = nonsignificant. (B) Representative images showing autophagy in macrophage cells in response to g-C_3N_4: RAW264.7 cells overexpressing mRFP-LC3 were incubated with Por g-C_3N_4 at concentrations of 5 µg mL^{-1} or 30 µg mL^{-1}. Confocal microscopy images of cells were acquired after 12 and 24 h of incubation. Scale bar: 10 µm. (C) Graph representing changes in autophagy in macrophage cells in response to 30 µg mL^{-1} g-C_3N_4: RAW264.7 cells overexpressing mRFP-LC3 were incubated with Exf and Por g-C_3N_4 at the concentration of 30 µg mL^{-1}. Confocal microscopy images of cells were acquired after 12 and 24 h of incubation and quantified using ImageJ for the number of mRFP-LC3 dots in cells with internalized g-C_3N_4. For calculating the number of puncta per cell, experiments were performed in duplicates. A minimum of 25 cells were counted for each replicate. Statistical significance was calculated on the data from experimental replicates using a two-tailed unpaired *t*-test. *P < 0.05, **P < 0.01, ***P < 0.001, (P) **** < 0.0001, and ns = nonsignificant. Data are represented as mean ± SEM. (D) Immunoblots of extracts from RAW264.7 cells stably expressing GFP-LC3 treated with Por g-C_3N_4. Membranes were probed for GFP-LC3 to identify the signals for LC3 I and LC3 II. Effect of Por and Exf g-C_3N_4 nanosheets on nitric oxide and cytokine secretion: RAW 264.7 macrophages were treated with nanomaterials at 0.5 µg ml^{-1}, 5 µg ml^{-1}, and 50 µg ml^{-1} concentrations for 24 h. (E) Nitric oxide assay was performed using Griess reagent. (F) IL-6 and (G) TNF-α cytokines were estimated by the sandwich ELISA method.

Por g-C_3N_4. This could be due to the lower aqueous dispersibility of Exf g-C_3N_4 compared to porous sheets.

Recently, immune cells such as neutrophils and macrophages have been reported to cause the degradation of nanomaterials upon their activation, and some materials (h-BN, GO, *etc.*) induce autophagy activation.[6,7,39,40] Notably, induction of autophagy by nanomaterials (but not cytotoxic) could be redirected for therapeutic applications such as eliminating toxic cellular components like aggregates, target tumour cells, *etc.*[41–43] Thus, to analyze the effect of immune cells on nanoparticles, RAW 264.7 macrophages were incubated with Exf or Por g-C_3N_4 sheets. The RAW 264.7 macrophage cells interna-

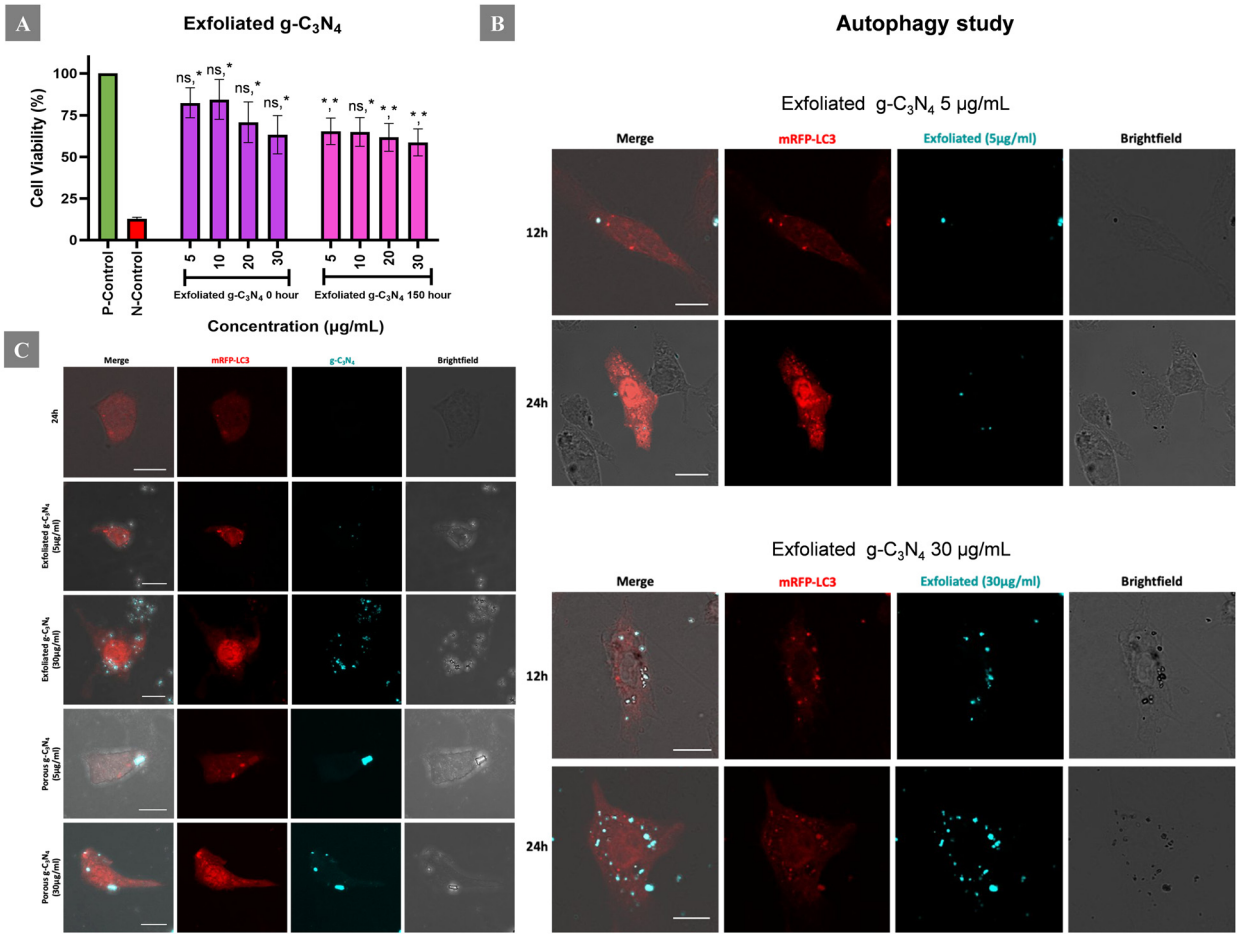

Fig. 7 (A) Cytotoxicity MTT study of Exf g-C_3N_4 before and after degradation at four different concentrations 5, 10, 20 and 30 μg mL^{-1} performed on RAW264.7 macrophage cell lines. Data are shown as mean ± standard deviation. Statistical significance was tested with a two-tailed, paired Student's test and is represented for each concentration *vs.* positive control (left side) and each concentration *vs.* negative control (right side). *P < 0.05, **P < 0.01, and ***P < 0.001. (B) Representative images showing autophagy in macrophage cells in response to g-C_3N_4: RAW264.7 cells overexpressing mRFP-LC3 were incubated with Exf g-C_3N_4 at the concentration of 5 μg mL^{-1} or 30 μg mL^{-1}. Confocal microscopy images of cells were acquired after 12 and 24 h of incubation. Scale bar: 10 μm. (C) Representative images showing autophagy in macrophage cells: RAW264.7 cells overexpressing mRFP-LC3 were kept untreated or were incubated with Exf or Por g-C_3N_4 at the concentrations of 5 μg mL^{-1} and 30 μg mL^{-1}. Z stack images of cells up-taking the compound were acquired using confocal microscopy. Scale bar: 10 μm.

lized both sheets, as demonstrated by their uptake after 6 h of incubation (Fig. 7C). One of the ways that cells eliminate intracellular components targeted for degradation is by employing autophagy.[44] Microtubule-associated protein 1A/1B-light chain 3 (LC3) protein is a soluble protein and one of the critical biomarkers of autophagy.[45,46] Thus, to analyze the onset of autophagy in RAW264.7 cells in response to g-C_3N_4, mRFP-LC3 was transiently overexpressed in RAW264.7 cells. It was found that macrophage cells sequestered mRFP-LC3-positive dots in response to Por and Exf g-C_3N_4 (Fig. 6B & 7B). These observations were further quantified by measuring the number of LC3 puncta per cell (Fig. 6C). The LC3 protein undergoes lipidation and converts from LC3 I to LC3 II (conjugated to phosphatidylethanolamine) upon autophagy initiation and autophagosome membrane formation.[46] Since the cell viability was higher in cells incubated with Por g-C_3N_4, RAW264.7 cells, stably expressing GFP-LC3, were incubated with Por g-C_3N_4 and then immunoblotted for the expression of GFP-LC3. As compared to the control, where only one band corresponding to GFP-LC3 I was detected, cells incubated with Por g-C_3N_4 showed higher levels of GFP-LC3 II (Fig. 6D and Fig. S10 (ESI†)). This indicated that g-C_3N_4 in the porous form led to the onset of autophagy in RAW264.7 macrophages.

Cytokine analysis of porous and exfoliated g-C_3N_4 sheets on macrophages

Macrophages are key elements of the innate immune system that perform various functions, including phagocytosis, regulation of inflammatory responses and modulation of the tumour microenvironment. Based on the stimuli, macrophages differentiate into diverse functional phenotypes, such as M1 and M2, resulting in the secretion of pro-inflammatory and anti-inflammatory cytokines. Given that g-C_3N_4 induces cellular autophagy, we intended to identify the vital signalling

pathways affected in macrophages.[47–49] We used RAW 264.7 macrophages to assess the effect of nanomaterials on NO and cytokine production. Lipopolysaccharide (LPS, 100 ng mL^{-1}) was used as a positive control to induce inflammation in macrophages, resulting in the production of pro-inflammatory cytokines and NO. Fig. 6E, F and G demonstrate that the Por g-C_3N_4 sheet-treated cells produced increased NO, IL-6 and TNF-α in a dose-dependent manner. However, the effect of Exf g-C_3N_4 sheets on the expression of NO decreased with increasing concentration, and the expression of all other cytokines was not detectable (Fig. S11†).

Conclusions

In summary, we successfully demonstrated that chemically resistant g-C_3N_4 nanosheets (both types such as ultra-thin or exfoliated and partially oxidized or porous sheets) could be degraded by the enzymatic action of human myeloperoxidase (hMPO) secreted by activated immune cells (neutrophils and macrophages). Next, environmental degradation of g-C_3N_4 sheets is reported using the plant peroxidase (HRP). Finally, the degradation of g-C_3N_4 sheets was also demonstrated by the UV-catalysed PF reaction, which generated hydroxy radicals, mimicking the intracellular environment under stress. The degradation of the nanosheets was confirmed by HR-TEM, Raman analysis, UV-visible absorption, fluorescence spectroscopy and XPS. Mass spectrometric analyses suggested the plausible degradation by-products produced during the PF-mediated oxidation. Furthermore, the cell cytotoxicity of pristine g-C_3N_4 sheets and the degraded samples revealed that the exfoliated sheets were slightly more toxic than the porous sheets due to the lower aqueous dispersibility of the exfoliated sheets. Interestingly, the Por g-C_3N_4 sheets induced the onset of autophagy in RAW264.7 macrophages, as confirmed by the quantification of LC3 I and LC3 II proteins that are markers for autophagy initiation and autophagosome membrane formation. The porous nanosheets exhibited a pro-inflammatory response through autophagy-induced nitric oxide, IL-6 and TNF-α production.

Author contributions

K. Swetha: synthesis of graphitic carbon nitride and characterization, biodegradation studies, methodology and analysis, data collection, writing the original draft and validation. P. Ganesh: photo-Fenton reaction, data collection and analysis. A. Kamath: mass-spectrometry analysis, data collection and analysis. A. Bhatnagar, M. Lakavathu, S. M. Srinivasula: autophagy induction, optimizing the bioassays and data collection and validation, writing the original manuscript and validation. P. Poornima and S. R. Bonam: immune cell interactions and cytotoxicity, manuscript writing and validation, R. Kurapati: project conceptualization, investigation, review and editing, draft, project administration and funding acquisition.

Data availabiltiy

The data supporting this article have been included as part of the ESI.†

Conflicts of interest

There are no conflicts to declare.

Acknowledgements

R. K. sincerely thanks the Science and Engineering Research Board (SERB), India, for financial support through the Start-up Research Grant (SRG/2022/000291); and the Department of Biotechnology (DBT) India, for the financial support through awarding DBT-RLS fellowship (BT/RLF/Re-entry/20/2020). The authors sincerely thank Mr. Livin Paul and Prof. K. George Thomas, School of Chemistry, IISER TVM, for their valuable assistance with Raman analysis. The authors thank Ms. Deepika Divakaran for her immense support in biological studies, and Mr. Alex, Mr. Pradeep and Mr. Krishna Kumar for their support in TEM, XPS and Mass analyses. K. Swetha also acknowledges funding for her PhD from the DST-INSPIRE Fellowship by Govt. India. The authors also acknowledge Prof. R. S. Swathi and Mr. Nandu for their support in understanding the interaction between nanomaterials and enzymes. SRB would like to thank the director of the Indian Institute of Chemical Technology, Hyderabad, for providing infrastructure, lab space, and support for the Institutional Research Grant (MLP9033). R. K. sincerely thank the IISER TVM and Hon'ble Director, Prof. J N Moorthy, for the excellent research support and infrastructure.

References

1 T. Reiss, K. Hjelt and A. C. Ferrari, Graphene is on track to deliver on its promises, *Nat. Nanotechnol.*, 2019, **14**(10), 907–910.
2 S. Vranic, R. Kurapati, K. Kostarelos and A. Bianco, Biological and environmental degradation of two-dimensional materials, *Nat. Rev. Chem.*, 2025, 173–184.
3 G. P. Kotchey, B. L. Allen, H. Vedala, N. Yanamala, A. A. Kapralov, Y. Y. Tyurina, J. Klein-Seetharaman, V. E. Kagan and A. Star, The Enzymatic Oxidation of Graphene Oxide, *ACS Nano*, 2011, **5**(3), 2098–2108.
4 R. Kurapati, J. Russier, M. A. Squillaci, E. Treossi, C. Ménard-Moyon, A. E. Del Rio-Castillo, E. Vazquez, P. Samorì, V. Palermo and A. Bianco, Dispersibility-Dependent Biodegradation of Graphene Oxide by Myeloperoxidase, *Small*, 2015, **11**(32), 3985–3994.

5 K. Swetha, S. Sudeshna, F. A. L. S. Silva, F. C. Silva, B. Freitas, J. A. C. Incorvia, J. R. Fernandes, A. Jayaraj, S. Banerjee, N. Sadananda Singh, F. D. Magalhães, A. M. Pinto and R. Kurapati, Biodegradability of Partially Reduced Nanographene Oxide by Human, Plant and Microbial Enzymes: Impact of Magnetic Nanoparticles, *Carbon*, 2024, **229**, 119486.

6 X. Luan, C. Martín, P. Zhang, Q. Li, I. A. Vacchi, L. G. Delogu, Y. Mai and A. Bianco, Degradation of Structurally Defined Graphene Nanoribbons by Myeloperoxidase and the Photo-Fenton Reaction, *Angew. Chem., Int. Ed.*, 2020, **59**(42), 18515–18521.

7 R. Kurapati, S. P. Mukherjee, C. Martín, G. Bepete, E. Vázquez, A. Pénicaud, B. Fadeel and A. Bianco, Degradation of Single-Layer and Few-Layer Graphene by Neutrophil Myeloperoxidase, *Angew. Chem., Int. Ed.*, 2018, **57**(36), 11722–11727.

8 R. Kurapati, C. Backes, C. Ménard-Moyon, J. N. Coleman and A. Bianco, White Graphene undergoes Peroxidase Degradation, *Angew. Chem., Int. Ed.*, 2016, **55**(18), 5506–5511.

9 P. Kurungottu, M. B. Thomas, M. M. Lalitha, P. Ganesh, D. P. Gnanadhas, D. Chakravortty, A. M. Raichur and R. Kurapati, Biodegradable Nanocomposite of ZnS(Mn) Quantum Dots Immobilized Graphene Oxide for Bioimaging Applications, *Nanotheranostics*, 2024, **8**(2), 150–162.

10 R. Kurapati, C. Martìn, V. Palermo, Y. Nishina and A. Bianco, Biodegradation of graphene materials catalyzed by human eosinophil peroxidase, *Faraday Discuss.*, 2021, **227**(0), 189–203.

11 F. T. Andõn, A. A. Kapralov, N. Yanamala, W. Feng, A. Baygan, B. J. Chambers, K. Hultenby, F. Ye, M. S. Toprak, B. D. Brandner, A. Fornara, J. Klein-Seetharaman, G. P. Kotchey, A. Star, A. A. Shvedova, B. Fadeel and V. E. Kagan, Biodegradation of single-walled carbon nanotubes by eosinophil peroxidase, *Small*, 2013, **9**(16), 2721–2729.

12 B. Ma, C. Martín, R. Kurapati and A. Bianco, Degradation-by-design: how chemical functionalization enhances the biodegradability and safety of 2D materials, *Chem. Soc. Rev.*, 2020, **49**(17), 6224–6247.

13 K. Swetha, A. Camisasca, M. Bartkowski, A. Garhwal, A. Aravind, P. Gnanadhas, S. Giordani and R. Kurapati, Biodegradability of Carbon Nano-Onions by Human Myeloperoxidase and Photo-Fenton Process, *ChemNanoMat*, 2024, **10**(6), e202300630.

14 B. Fadeel, C. Bussy, S. Merino, E. Vázquez, E. Flahaut, F. Mouchet, L. Evariste, L. Gauthier, A. J. Koivisto, U. Vogel, C. Martín, L. G. Delogu, T. Buerki-Thurnherr, P. Wick, D. Beloin-Saint-Pierre, R. Hischier, M. Pelin, F. Candotto Carniel, M. Tretiach, F. Cesca, F. Benfenati, D. Scaini, L. Ballerini, K. Kostarelos, M. Prato and A. Bianco, Safety Assessment of Graphene-Based Materials: Focus on Human Health and the Environment, *ACS Nano*, 2018, **12**(11), 10582–10620.

15 R. Kurapati, L. Muzi, A. P. R. de Garibay, J. Russier, D. Voiry, I. A. Vacchi, M. Chhowalla and A. Bianco, Enzymatic Biodegradability of Pristine and Functionalized Transition Metal Dichalcogenide MoS2 Nanosheets, *Adv. Funct. Mater.*, 2017, **27**, 1605176.

16 H. Lin, S. Gao, C. Dai, Y. Chen and J. Shi, A Two-Dimensional Biodegradable Niobium Carbide (MXene) for Photothermal Tumor Eradication in NIR-I and NIR-II Biowindows, *J. Am. Chem. Soc.*, 2017, **139**(45), 16235–16247.

17 J. Kaur, K. Swetha, M. Singh, A. Abduvakhidov, M. Varra, M. Lakavathu, J. Adam, A. Prajapati, S. R. Bonam, C. Altucci and R. Kurapati, Functionalization dependent biodegradability of two-dimensional antimonene by peroxidases: impact on immune modulation, *Nanoscale*, 2025, 11293–11304.

18 K. Sharma, A. Sudhaik, P. Raizada, P. Thakur, X. M. Pham, Q. Van Le, V.-H. Nguyen, T. Ahamad, S. Thakur and P. Singh, Constructing α-Fe2O3/g-C3N4/SiO_2 S-scheme-based heterostructure for photo-Fenton like degradation of rhodamine B dye in aqueous solution, *Environ. Sci. Pollut. Res.*, 2023, **30**(60), 124902–124920.

19 X. Zhang, X. Xie, H. Wang, J. Zhang, B. Pan and Y. Xie, Enhanced Photoresponsive Ultrathin Graphitic-Phase C3N4 Nanosheets for Bioimaging, *J. Am. Chem. Soc.*, 2013, **135**(1), 18–21.

20 G. Liao, Y. Gong, L. Zhang, H. Gao, G.-J. Yang and B. Fang, Semiconductor polymeric graphitic carbon nitride photocatalysts: the "holy grail" for the photocatalytic hydrogen evolution reaction under visible light, *Energy Environ. Sci.*, 2019, **12**(7), 2080–2147.

21 A. Thomas, A. Fischer, F. Goettmann, M. Antonietti, J.-O. Müller, R. Schlögl and J. M. Carlsson, Graphitic carbon nitride materials: variation of structure and morphology and their use as metal-free catalysts, *J. Mater. Chem.*, 2008, **18**(41), 4893–4908.

22 Q. Xiang, B. Cheng and J. Yu, Hierarchical porous CdS nanosheet-assembled flowers with enhanced visible-light photocatalytic H2-production performance, *Appl. Catal., B*, 2013, **138–139**, 299–303.

23 Z.-T. Jiang, J. Chen, F.-Y. Chen, Y.-Q. Cheng, S.-Y. Yao, R. Ma, W.-B. Li, H. Chen and D.-S. Guo, A FRET Autophagy Imaging Platform by Macrocyclic Amphiphile, *Angew. Chem., Int. Ed.*, 2025, **64**, e202420793.

24 Y. Li, T. Gong, H. Gao, Y. Chen, H. Li, P. Zhao, Y. Jiang, K. Wang, Y. Wu, X. Zheng and W. Bu, ZIF-Based Nanoparticles Combine X-Ray-Induced Nitrosative Stress with Autophagy Management for Hypoxic Prostate Cancer Therapy, *Angew. Chem., Int. Ed.*, 2021, **60**(28), 15472–15481.

25 S. Wang, Z. Wang, Z. Zang, X. Liang, B. Jia, T. Ye, Y. Lan and X. Shi, A Mitochondrion-Targeting Piezoelectric Nanosystem for the Treatment of Erectile Dysfunction via Autophagy Regulation, *Adv. Mater.*, 2025, **37**(5), e2413287.

26 G.-Y. Chen, C.-L. Chen, H.-Y. Tuan, P.-X. Yuan, K.-C. Li, H.-J. Yang and Y.-C. Hu, Graphene Oxide Triggers Toll-Like Receptors/Autophagy Responses In Vitro and Inhibits Tumor Growth In Vivo, *Adv. Healthcare Mater.*, 2014, **3**(9), 1486–1495.

27 H.-J. Li, B.-W. Sun, L. Sui, D.-J. Qian and M. Chen, Preparation of water-dispersible porous g-C3N4 with improved photocatalytic activity by chemical oxidation, *Phys. Chem. Chem. Phys.*, 2015, **17**(5), 3309–3315.
28 J. Jiang, L. Ou-yang, L. Zhu, A. Zheng, J. Zou, X. Yi and H. Tang, Dependence of electronic structure of g-C3N4 on the layer number of its nanosheets: A study by Raman spectroscopy coupled with first-principles calculations, *Carbon*, 2014, **80**, 213–221.
29 C. C. Winterbourn and A. J. Kettle, Biomarkers of myeloperoxidase-derived hypochlorous acid, *Free Radicals Biol. Med.*, 2000, **29**(5), 403–409.
30 M. I. Chebanenko, L. A. Lebedev, V. L. Ugolkov, N. D. Prasolov, V. N. Nevedomskiy and V. I. Popkov, Chemical and structural changes of g-C3N4 through oxidative physical vapor deposition, *Appl. Surf. Sci.*, 2022, **600**, 154079.
31 G. P. Kotchey, S. A. Hasan, A. A. Kapralov, S. H. Ha, K. Kim, A. A. Shvedova, V. E. Kagan and A. Star, A natural vanishing act: The enzyme-catalyzed degradation of carbon nanomaterials, *Acc. Chem. Res.*, 2012, **45**(10), 1770–1781.
32 X. Zhou, Y. Zhang, C. Wang, X. Wu, Y. Yang, B. Zheng, H. Wu, S. Guo and J. Zhang, Photo-Fenton Reaction of Graphene Oxide: A New Strategy to Prepare Graphene Quantum Dots for DNA Cleavage, *ACS Nano*, 2012, **6**(8), 6592–6599.
33 F. Qiao, J. Wang, S. Ai and L. Li, As a new peroxidase mimetics: The synthesis of selenium doped graphitic carbon nitride nanosheets and applications on colorimetric detection of H_2O_2 and xanthine, *Sens. Actuators, B*, 2015, **216**, 418–427.
34 A. Vinu, Two-Dimensional Hexagonally-Ordered Mesoporous Carbon Nitrides with Tunable Pore Diameter, Surface Area and Nitrogen Content, *Adv. Funct. Mater.*, 2008, **18**(5), 816–827.
35 S. Kailasa and H.-F. Wu, Electrospray Ionization Tandem Mass Spectrometry for Rapid, Sensitive and Direct Detection of Melamine in Dairy Products, *J. Ind. Eng. Chem.*, 2015, **21**, 138–144.
36 K. Chingin, R. H. Perry, S. D. Chambreau, G. L. Vaghjiani and R. N. Zare, Generation of Melamine Polymer Condensates upon Hypergolic Ignition of Dicyanamide Ionic Liquids, *Angew. Chem., Int. Ed.*, 2011, **50**(37), 8634–8637.
37 S. J. Makowski, P. Köstler and W. Schnick, Formation of a hydrogen-bonded heptazine framework by self-assembly of melem into a hexagonal channel structure, *Chemistry*, 2012, **18**(11), 3248–3257.
38 N. Lewinski, V. Colvin and R. Drezek, Cytotoxicity of Nanoparticles, *Small*, 2008, **4**(1), 26–49.
39 S. Mondal, C. P. Vinod and U. K. Gautam, 'Autophagy' and unique aerial oxygen harvesting properties exhibited by highly photocatalytic carbon quantum dots, *Carbon*, 2021, **181**, 16–27.
40 G. Gupta, Z. Wang, V. M. Kissling, A. Gogos, P. Wick and T. Buerki-Thurnherr, Boron Nitride Nanosheets Induce Lipid Accumulation and Autophagy in Human Alveolar Lung Epithelial Cells Cultivated at Air-Liquid Interface, *Small*, 2024, **20**(27), e2308148.
41 A. K. Sarkar, G. Kaur, P. Seth, N. R. Jana and N. R. Jana, Autophagy-Induced Nanoparticle-Based Clearing of Toxic Huntingtin Protein Aggregates from Neuron Cells, *ACS Appl. Nano Mater.*, 2024, **7**(3), 3468–3478.
42 X. Long, J. Yan, Z. Zhang, J. Chang, B. He, Y. Sun and Y. Liang, Autophagy-targeted nanoparticles for effective cancer treatment: advances and outlook, *NPG Asia Mater.*, 2022, **14**(1), 71.
43 I. Florance, M. Cordani, P. Pashootan, M. A. Moosavi, A. Zarrabi and N. Chandrasekaran, The impact of nanomaterials on autophagy across health and disease conditions, *Cell. Mol. Life Sci.*, 2024, **81**(1), 184.
44 D. J. Klionsky, The molecular machinery of autophagy: unanswered questions, *J. Cell Sci.*, 2005, **118**(Pt 1), 7–18.
45 E. L. Eskelinen, Maturation of autophagic vacuoles in Mammalian cells, *Autophagy*, 2005, **1**(1), 1–10.
46 Y. Kabeya, N. Mizushima, T. Ueno, A. Yamamoto, T. Kirisako, T. Noda, E. Kominami, Y. Ohsumi and T. Yoshimori, LC3, a mammalian homologue of yeast Apg8p, is localized in autophagosome membranes after processing, *EMBO J.*, 2000, **19**(21), 5720–5728.
47 A. Mayr, J. Marciniak, B. Eggers, K. Blawat, J. Wildenhof, R. Bastos Craveiro, M. Wolf, J. Deschner, A. Jäger and S. Beisel-Memmert, Autophagy Induces Expression of IL-6 in Human Periodontal Ligament Fibroblasts Under Mechanical Load and Overload and Effects Osteoclastogenesis in vitro, *Front Physiol.*, 2021, **12**, 716441.
48 E.-J. Lee, H.-J. Kim, M. S. Choi and J.-E. Chang, Crosstalk between Autophagy and Inflammatory Processes in Cancer, *Life (Basel)*, 2021, **11**(9), 903.
49 C. R. Pestana, J. C. Oishi, H. S. Salistre-Araújo and G. J. Rodrigues, Inhibition of Autophagy by Chloroquine Stimulates Nitric Oxide Production and Protects Endothelial Function during Serum Deprivation, *Cell. Physiol. Biochem.*, 2015, **37**(3), 1168–1177.

